Flow and stability analysis of a hypersonic boundary-layer over an axisymmetric cone-cylinder-flare configuration

Sébastien Esquieu, Elizabeth Benitez, Steven Schneider, Jean-Philippe Brazier

Flow and Stability Analysis of a Hypersonic Boundary Layer over an Axisymmetric Ccone-cylinder-flare Configuration

Sebastien Esquieu*
CEA, The French Alternative Energies and Atomic Energy Commission, Le Barp, France

Elizabeth Benitez,† Steven P. Schneider‡
School of Aeronautics and Astronautics, Purdue University, West Lafayette, Indiana, USA.

Jean-Philippe Brazier§
ONERA / DMPE, Université de Toulouse, F-31055 Toulouse - France

The stability of hypersonic boundary layer over an axisymmetric ccone-cylinder-flare configuration at Mach 6 and zero degree angle of attack is investigated for different Reynolds numbers. The shape has been designed for wind tunnel test experiments with two main goals: keep an attached boundary layer all along the object and investigate the effects of pressure gradients, flow expansion and recompression without flow separation, on the hypersonic boundary layer stability. After a thorough study of the aerodynamic flow obtained in fully laminar conditions, linear stability theory (LST) and linear parabolized stability equations (PSE) are used to predict the amplification rates of the boundary layer disturbances. The stability analyses are performed with the 2D-axisymmetric version of the STABL software suite from the Univerity of Minnesota in LST and PSE modes. Code comparisons with the ONERA Mamout solver are also realized in LST mode. The numerical stability results are compared to wind tunnel measurements obtained in the BAM6QT (Boeing AFOSR Mach-6 Quiet Tunnel) wind tunnel of Purdue University. The semi-empirical e^N method allows to correlate transition with the integrated growth of the linear instability waves. Finally, the computed N factors which correspond roughly to wave amplitude are compared to measured power spectra.

I. Nomenclature

$Mach$	=	Mach number
pi	=	stagnation pressure (bar)
Ti	=	stagnation temperature (K)
Hi	=	total enthalpy (J/kg)
p	=	mean pressure (Pa)
T	=	static temperature (K)
ρ	=	density (kg/m^3)
u,v,w	=	velocity in x,y,z directions (m/s)
V	=	velocity magnitude
$Re_{/m}$	=	freestream unit Reynolds number (1/m)
x	=	geometric coordinate in streamwise direction (m)
y	=	geometric coordinate in body-normal direction (m)
z	=	geometric coordinate in spanwise direction (m)
Rn	=	nose radius (m)
δ	=	boundary layer thickness (m)
α_i	=	amplification rate (1/m)
ψ	=	wave propagation angle (^{o})

*Aerospace Engineer.
†PhD Student.
‡Professor, Fellow AIAA
§Aerospace Engineer.

Subscripts

∞ = value in freestream
e = value at the boundary layer edge

II. Introduction

The laminar-to-turbulent transition is a primordial input for trajectory and conceptional design of hypersonic objects. Indeed, transition at hypersonic speeds causes large changes in heat transfer, skin friction and boundary layer separation. Turbulent boundary layers increase the heating rate and the viscous drag, and offer a greater resistance to the formation of separation bubble. As a consequence, the aerodynamic lift and drag, the stability and control of the object as well as the thermal protection system are directly affected by the state of the boundary layer. So the knowledge of stability and transition of high-speed boundary layer is an important issue for hypersonic flights. But understanding how and where transition occurs on a given configuration during re-entry or high speed flight is one of the long-standing problems in aerodynamics (Leyva [1]).

In flight or in a wind tunnel, disturbances are present in the flow and interact with the boundary layer that develops along the object. The boundary layer acts as a selective filter where only certain frequencies and wavelengths of those disturbances can be amplified and eventually induce a laminar-to-turbulent transition. For a small disturbance environment, as explained by Stetson [2], four fundamentally different instability mechanisms can produce disturbance growth in a hypersonic boundary layer: first-mode, second-mode, crossflow instabilities and Görtler vortices. Several paths to transition exist (Morkovin, [3]) but, here, only the low disturbance level is considered where eigenmode growth is dominant.

As detailed by Schneider [4], the first-mode instability is similar to low-speed Tollmien-Schlichting waves and occurs for subsonic and moderate supersonic flows. It is most amplified when the wavefronts are oblique to the stream direction. The second-mode instability concerns hypersonic flows. It is similar to a trapped acoustic wave and is most amplified when the wavefronts are normal to the stream direction. The cross-flow instability occurs in three-dimensional boundary layers, and has both traveling and stationary forms. The Gortler instability is important for boundary layers on concave walls, and perhaps in some regions of concave streamline curvature.

Very instructive and thorough studies of the transition development are available for attached boundary layer mainly on cone shapes [5] [6]. Here the ccone-cylinder-flare configuration allows to add the influence of pressure gradients, flow expansion and compression, on the boundary layer stability. This shape, specially designed for this study, is made so that the flow experiences a limited positive pressure gradient on the flare. This allows to keep an attached boundary layer on the aft-cylinder and on flare. Indeed, a larger flare angle would generate a flow separation which represents an even more challeging case. This complex case of instability development in the presence of a separation bubble could be addressed in the framework of a future stability analysis study.

The hypersonic flows addressed here are considered in wind tunnel conditions at Mach 6. In these high speed conditions and with the quasi-sharp cone cylinder shape, the edge Mach number will be greater than Mach 5 all along the configuration. Following Mack's theory [7], in this case the dominant instabilities will be the second-mode mode waves. Görtler instabilities could also be present in the concave part of the geometry but here the flare angle is very limited and these instabilities should not be predominant.

Görtler instabilities should be taken into account in the transition process for flow separated cases such as the hollow cylinder flare configuration studied by Benay and Bur [8] [9] . The present shape but with a larger flare angles would generate a flow separation and in this case both second-mode and Görtler instabilities should be considered simultaneously. In the present study, with attached boundary layer only, the focus is mainly on the two-dimensional second-mode waves.

The second-mode instability waves are investigated from the numerical point of view thanks to the boundary layer stability computations, and also with wind tunnel experiments with high-frequency pressure sensor measurements. The

numerical part is realized thanks to two stability codes, the STABL software suite from the University of Minnesota [10] and the Mamout code from ONERA. The hypersonic experiments are conducted in the Boeing/AFOSR Mach-6 Quiet Tunnel (BAM6QT) of Purdue University [11].

III. Ccone-cylinder-flare geometry

An axisymmetric ccone-cylinder-flare configuration was designed in order to promote transition development for an attached boundary layer flow with flow expansion and recompression in high speed flow. The main characteristics of the designed shape are the following:

1) small nose radius Rn = 0.1 mm ;
2) half-cone angle is equal to 5 degrees ;
3) flare angle is equal to 3.5 degrees.

The main dimensions of the ccone-cylinder-flare configuration are given in table 1:

Table 1 Model coordinates

	Nose-Cone junction	Cone-Cylinder junction	Cylinder-Flare junction	End of flare
x (m)	0.0920×10^{-3}	0.398147	0.525670	0.764456
y (m)	0.0997×10^{-3}	0.034925	0.034925	0.049530

IV. Structured grid

The initial grid is a single-block structured grid composed of 1009 points in the longitudinal direction and 301 points in the wall normal direction. Special care is given to the first cell size and to the point distribution in the wall normal direction in order to ensure a very accurate boundary layer calculation and also to capture correctly the shock all along the shape. The initial grid generated with ICEM-CFD can be qualified as very good quality (see figure 1a) but in order to ensure higher accuracy in the mean flow solution for the stability analysis, the shock tailoring procedure available in the STABL suite is used. This grid adaptation procedure allows to capture all the gradients more accurately by redistributing the grid points based on the initial converged solution (see figure 1b).

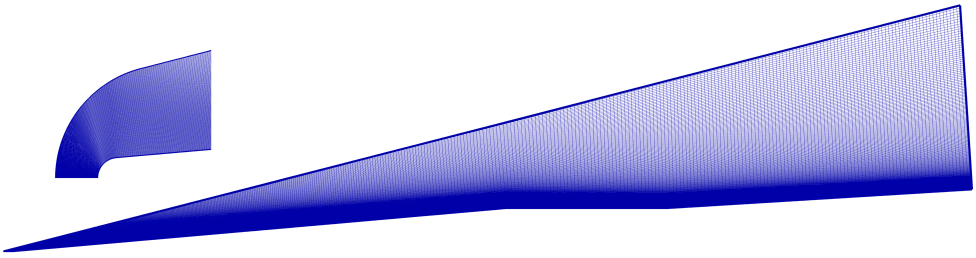

(a) Initial single-block structured grid (1009 x 301) - 303 709 grid points

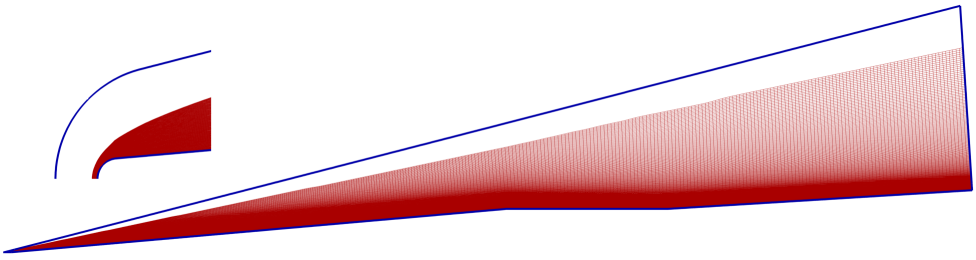

(b) Shock tailored grid obtained at $Re_{/m} = 5.57 \times 10^6$ - 1 block (1009x298) - 300 682 grid points

Fig. 1 Initial and tailored structured grids

V. CFD computations

A. Laminar mean flow computations

The laminar mean flow solutions for the stability analysis are performed with the axisymmetric CFD code provided with the STABL software suite written by Dr. Heath Johnson [10]. This axisymmetric flow solver DPLR2D uses a finite volume formulation and solves the reacting Navier-Stokes equations. The second-order inviscid fluxes are based on the modified Steger-Warming flux vector splitting method. The viscous fluxes are also second order accurate. The time integration method is the implicit first-order data parallel line relaxation (DPLR) method.

Since the aerodynamic flows considered here correspond to cold wind tunnel conditions in air, the gas mixture considered for the computation is non-reacting gas "Air" (perfect gas) and the effects of chemistry and molecular vibration are omitted for the calculations. The freestream aerodynamic conditions for the three considered cases are given in Table 2:

Table 2 Aerodynamic conditions

Case	Mach	pi (bar/psia)	Ti (K)	$Re_{/m}$	p_∞ (Pa)	T_∞ (K)	ρ_∞ (kg/m^3)	T_{wall} (K)	V_∞ (m/s)
1	6.0	2.59 / 37.5	430.	2.79x10^6	164.0	52.4	0.01090	300.	871.0
2	6.0	5.17 / 75.0	430.	5.57x10^6	327.5	52.4	0.02175	300.	871.0
3	6.0	10.34 / 150.0	430.	11.15x10^6	654.9	52.4	0.04351	300.	871.0

The viscosity law used is Sutherland's law and the heat conductivity is calculated using Eucken's relation. For the freestream temperature $T_\infty = 52.4K$, the molecular viscosity value is $\mu = 3.400\text{x}10^{-6} kg/(m.s)$ and and the heat conductivity value is $k_{cond} = 0.004627\ W/(m.K)$.

The laminar mean flow solutions obtained for the two extreme Reynolds number, $Re_{/m} = 2.79\text{x}10^6$ and $Re_{/m} = 11.15\text{x}10^6$, are presented respectively in figures 2a and 2b as pseudo-schlieren visualizations. The density gradient magnitude shows the bow shock generated from the small nose radius of 0.1 mm, the boundary layer with a sensitive increase on the cylinder due to the flow expansion and finally the recompression shock at the cylinder flare junction which leads to a decrease of the boundary layer thickness. A clear Reynolds number effect is visible on these figures; the boundary layer is far thicker at $Re_{/m}$=2.79x10^6 compared to $Re_{/m}$=11.15x10^6.

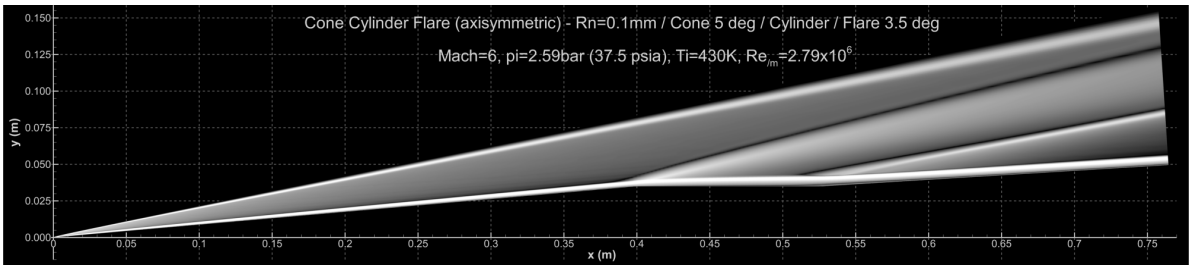

(a) Fully laminar computation at $Re_{/m}$ = 2.79x10^6

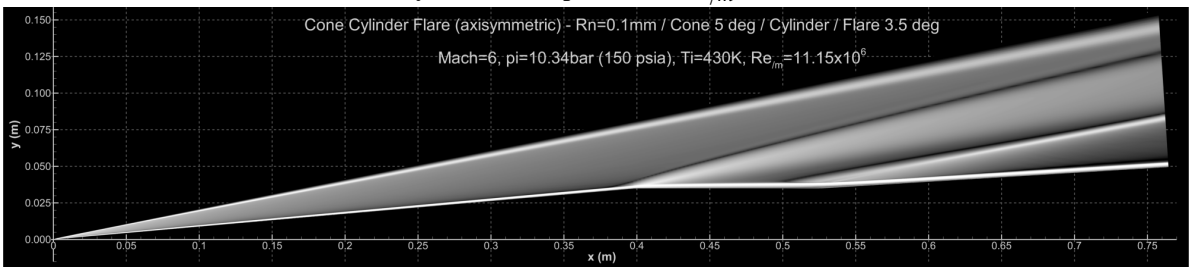

(b) Fully laminar computation at $Re_{/m}$ = 11.15x10^6

Fig. 2 Density gradient magnitude on the ccone-cylinder-flare configuration

B. Flow analyis

1. Flow around the nose

From a stability analysis point of view, it is known that the increase of the bluntness of the nose (till a certain limit) has a stabilizing effect on the boundary layer [12] [13]. Indeed, in hypersonic flow, increasing nose bluntness pushes back the point where second-mode disturbances become active. Here, the cone has a quasi-sharp nose ($R_n = 0.1mm$) so such a small nose radii will have a limited consequence on the boundary layer stability knowing also the entropy swallowing distance is very limited. Nevertheless, for the accuracy of the stability analysis study, it was decided to give special attention to the nose region in the computations.

For this perfect-gas flow, the Mach number distribution around the stagnation point is presented in figures 3a and 3b for two extreme Reynolds numbers considered here $\mathrm{Re}_{/m} = 2.79\mathrm{x}10^6$ and $\mathrm{Re}_{/m} = 11.15\mathrm{x}10^6$.

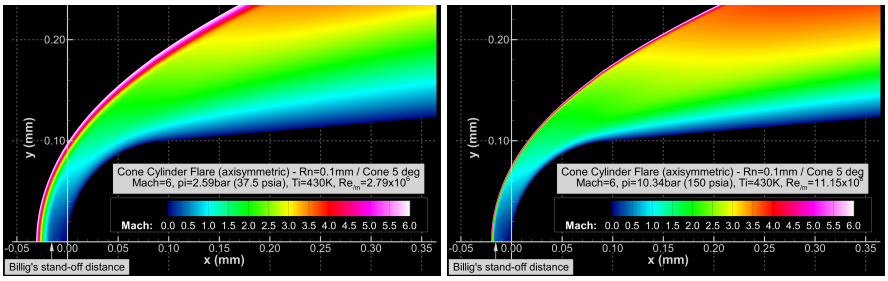

(a) $\mathrm{Re}_{/m} = 2.79\mathrm{x}10^6$ **(b) $\mathrm{Re}_{/m} = 11.15\mathrm{x}10^6$**

Fig. 3 Mach number distribution around the nose

From a quantitative point of view, the shock stand-off distance Δ can be compared to the Billig's empirical formula for sphere-cone shapes:

$$\Delta/R_n = 0.143exp(3.24/M_\infty^2)$$

Here with $R_n = 0.1mm$, the shock detachment evaluated with Billig's formula is equal to $\Delta = 0.0156mm$. This stand-off distance, plotted in figures 3a and 3b, highlights the physical Reynolds number effect on the shock layer thickness. A decrease in thickness of the shock layer due the increase of density is clearly visible at $\mathrm{Re}_{/m} = 11.15\mathrm{x}10^6$ when compared to $\mathrm{Re}_{/m} = 2.79\mathrm{x}10^6$. As a consequence, a better agreement is logically observed between the higher Reynolds number considered here and the Billig's empirical stand-off distance.

The thermal environment around the nose is due to the conversion of the kinetic energy associated with hypersonic flight. As shown in figures 4a and 4b, this conversion, due to the high compression and viscous energy dissipation mechanisms around this stagnation region, leads into increasing temperature around the blunt nose as explained by Bertin [14]. The isothermal wall temperature equal to 300 K explains the decrease of temperature near the wall.

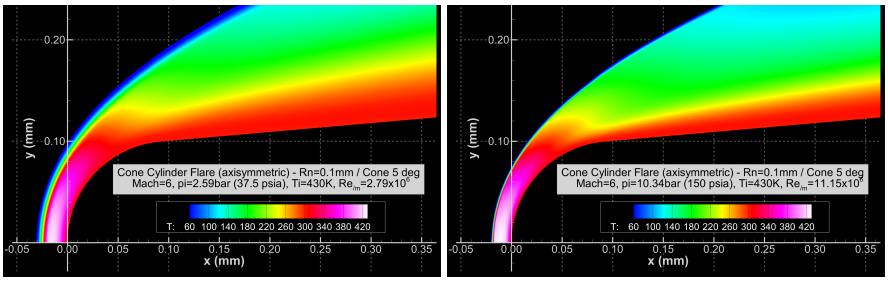

(a) $\mathrm{Re}_{/m} = 2.79\mathrm{x}10^6$ **(b) $\mathrm{Re}_{/m} = 11.15\mathrm{x}10^6$**

Fig. 4 Temperature distribution around the nose

The high gradients around the nose are very accurately captured by the computations so the influence of this very small bluntness is thoroughly defined for the stability analysis.

2. ***Pressure and skin friction***

On this ccone-cylinder-flare geometry, the flow encounters not only the classical quasi-constant pressure level on the cone but also experiences pressure gradients further downstream: firstly a favorable pressure gradient on the cylinder and secondly an adverse pressure gradient on the flare as shown in figure 5a.

The skin friction constantly diminishes on the cone and, after a narrow peak at cone-cylinder junction, experiences a new significant decrease on the cylinder (see figure 5b). The minimum skin friction value at the cone-flare junction is followed by a slight and progressive increase on the flare.

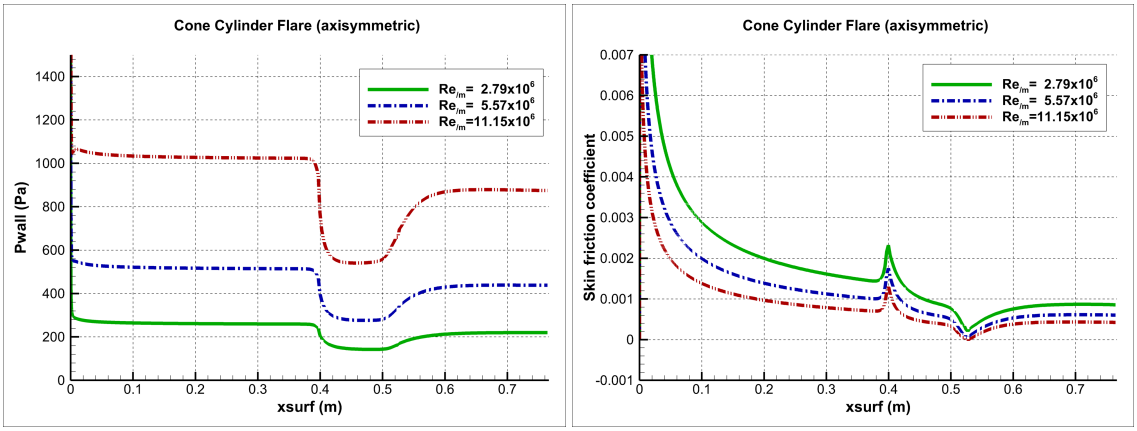

(a) Pressure distribution **(b) Skin friction coefficient**

Fig. 5 Pressure distribultion and skin friction as a function of Reynolds number

Near the cylinder-flare junction the flow faces the adverse pressure gradient due to the presence of the flare. This generates a dynamic situation where the flux of the incoming fluid momentum will eventually be balanced by the force and the flow will be brought to rest [15]. In this situation, a sufficient pressure gradient will lead to a flow separation. Here the shape has been designed with a small flare angle in order to generate a limited adverse pressure gradient so that no separation bubble appears. Here it is confirmed that the boundary layer is still attached. It can be noticed nevertheless that the skin friction coefficient is close to zero at the cylinder-flare junction and is even at zero for the case at $\mathrm{Re}_{/m} = 11.15\mathrm{x}10^6$. The addition of the wall shear stress and the positive pressure increase is not sufficient to generate a backflow region but it can be stated that any increase of the flare angle will lead to the formation of a separation bubble.

These favorable and adverse pressure gradients will have an influence on the boundary layer stability: it is known that the expansion has a stabilizing effect while the compression has a destabilizing impact. The aim of this study consists in evaluating the effects of these pressure gradients on the second-mode instability development along the object.

3. ***Boundary layer properties and edge Mach number***

The boundary layer detection is never a trivial calculation for hypersonic flows. Here the detection is based on the "Return from enthalpy overshoot" criterion. After detecting the total enthalpy peak in the boundary layer profile, the algorithm moves away from the wall until the total enthalpy has returned to a value near the freestream one. For this criterion, the total enthalpy at the boundary layer edge satisfies:

$$Hi_e < \frac{Hi_\infty - Hi_{wall}}{0.995} + Hi_{wall}$$

A detailed analysis of the STABL edge detection algorithms is available in [16]).

After careful checks, this boundary layer edge detection method appears well suited and accurate for the present cases which is mandatory for thorough analyses.

Whatever the Reynolds number considered, the general trend of the boundary layer thickness evolution is the same. After the classical increase of the boundary layer thickness along the cone, a new abrupt and large thickness increase appears on the cylinder because of the influence of the flow expansion generated at cone-cylinder junction. On the other hand, the adverse pressure gradient leads to an important decrease of the boundary layer thickness on the first half of the flare before a new slight increase of the boundary layer thickness further downstream (see figure 6a).

When considering the different Reynolds numbers computed here, it can be seen as expected that the boundary layer thickness decreases with the increase of Reynolds number: it goes from around 3.5 mm to 1.75 mm at the end of the cone for the two extreme Reynolds numbers and from around 7 mm to 3.5 mm on the aft part of the cylinder.

The edge Mach number values detected with the total enthalpy criterion in the computations are shown in figure 6b. . The value of $M_e \sim 5.5$ on the cone is in good agreement with the Taylor-Maccoll estimation of $M_e \sim 5.6$ for a 5-degrees half-angle nearly-sharp cone at a freestream Mach number of 6.0 at moderate Reynolds numbers. Downstream, the edge Mach number increases to around $M_e \sim 6.1$ on the cylinder due to the flow expansion and finally decreases to around $M_e \sim 5.65$ on the flare after the recompression at the cylinder flare junction.

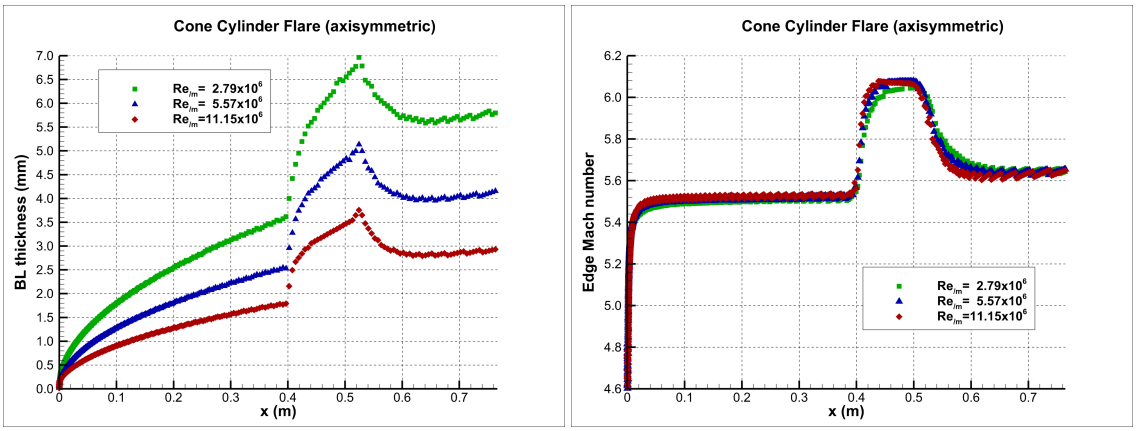

(a) Boundary layer thickness **(b) Edge Mach number**

Fig. 6 Boundary layer thickness and edge Mach number as a function of Reynolds number

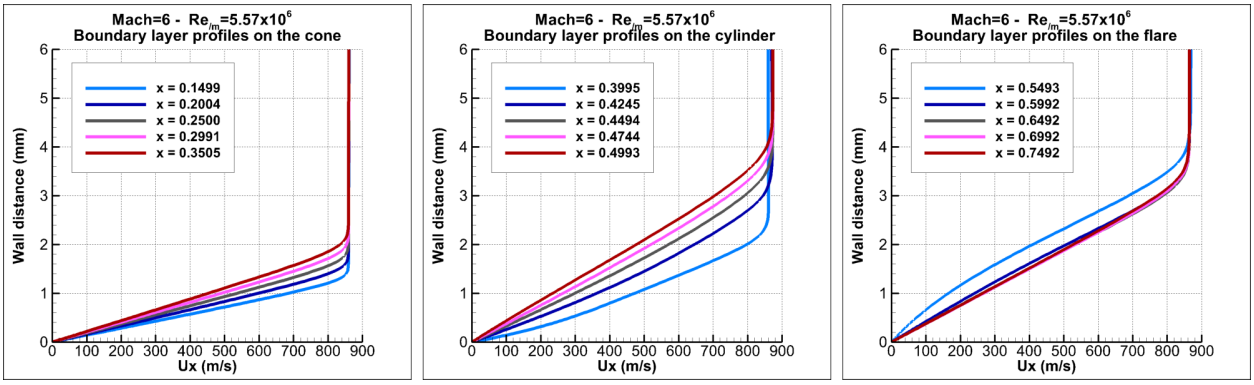

Fig. 7 Boundary layer profiles on the configuration at $Re_{/m}$ = 5.57x10^6

It is known that the 2^{nd} mode instabilities grow more rapidly at high Mach number values and on cold walls. Here,

the high edge Mach number and the limited wall temperature ($T_{wall} \sim 300K$) suggest that the second-mode waves will be the dominant instability as stated by Mack's theory [7]. Furthermore, knowing that second-mode instability frequencies are directly linked to the boundary layer thickness, it can be guessed that very different frequencies will be amplified on the different part of the object.

The boundary layer profiles that develop on the cone, on the cylinder (accelerated flow) and on the flare (decelerated flow) are shown in figure 7 for the computation at $Re_{/m}$=5.57x10^6. The shapes of the profiles are dramatically different on the three parts of the object. As a consequence, it can be guessed that the impact on the boundary layer stability will be important.

*4. **Second-mode wave instabilities***

Mack [7] found that the major instability waves leading to transition to turbulence on a smooth flat plate in a perfect gas flow are the first and second modes. In a supersonic flow, the most unstable first-mode disturbance is always oblique (ψ=45-60°). The wave angle ψ of the most unstable disturbance increases rapidly with Mach number and is in the range from 55°-60° above Mach = 1.5. On the other hand, in hypersonic flows above an edge Mach number of 4.5, the second-mode is the most unstable and two-dimensional disturbances (ψ=0 °) are the most unstable.

Following the previous analysis and results, the second-mode should be the dominant instability here. The second-mode waves are acoustic instabilities propagating and growing inside the laminar boundary layer and their final breakdown lead to turbulent flow. The boundary layer behaves as an acoustic waveguide as indicated by Fedorov [17]. Knowing that the wavelength of the 2^{nd} mode instability is about twice the boundary layer thickness [18], the estimated second-mode instability frequency is calculated as:

$$f_{2nd\,mode} = \frac{V_e}{2\delta}$$

So for waves moving with the edge velocity ($V_e \sim 860m/s$), the estimated frequency of the second-mode wave disturbance will be respectively of the order of 240 kHz at the end of the cone for the thin boundary layer ($\delta \sim 1.8mm$) at $Re_{/m}$ =11.15x10^6 and 120kHz for the thicker one ($\delta \sim 3.6mm$) at $Re_{/m}$ = 2.79x10^6. On the aft part of the model, the second-mode frequency should be of the order of respectively 70 and 140 kHz for the two extreme Reynolds number considered here (with δ equal respectively to around 5.8 mm and 3.0 mm).

VI. Stability analyses

A. Stability analysis solvers

*1. **STABL***

The main part of the stability analyses are performed using the PSE-Chem solver, which is a part of the STABL software suite [10]. PSE-Chem solves the reacting, two-dimensional, axisymmetric, linear parabolized stability equations (PSE) to predict the amplification of disturbances as they interact with the boundary-layer. The PSE-Chem solver includes finite-rate chemistry and translational-vibrational energy exchange. Generally, a transition location is predicted using the semi-empirical e^N method, in which transition is assumed to occur when a disturbance has grown by a factor of e^N from its initial amplitude. The N-factor values commonly used to correlate transition to flight are between 8 to 11.

Both linear stability theory (LST) and PSE analyses were performed using the PSE-Chem code. For the LST analysis, a parallel flow assumption is made by neglecting derivatives of mean flow quantities in the direction of the computational coordinate along the body. The PSE is expected to be more accurate as it does not assume parallel flow, in this case linear stability theory is used to provide the initial wavenumber for the PSE marching procedure ([19]).

*2. **Mamout***

Stability analyses have also been carried out on the same configurations with the ONERA in-house code Mamout. This code solves the local linear stability equations for an incompressible fluid, an ideal gas or a chemical equilibrium mixture, with the parallel flow assumption. The present computations use the perfect gas model. The resulting

one-dimensional differential Eigenvalue problem can be solved thanks to several numerical schemes, among which Chebyshev polynomial collocation method or high-order compact schemes. The computational grid can be split in multiple sub-domains. Outside of the boundary layer, the fluctuation is matched to the analytical solution obtained for a uniform base flow.

B. Stability analysis results

The same DPLR2D laminar flow solutions are used as input for STABL and Mamout stability analyses.

The second-mode disturbances are highly "tuned" to the boundary layer thickness resulting in considerable selectivity in the disturbance frequencies which are most amplified [2]. Seeing the boundary layer thickness evolution shown in figure 6a, it has been stated that the thin boundary layer on the cone will generate higher frequency disturbances than the thicker boundary layer on the cylinder and on the flare. Here, another aerodynamic effect will impact the boundary layer stability: the pressure gradients generated respectively on the cylinder and on the flare.

1. Amplification rates

All the stability diagrams presented in figures 8 and 9 for different Reynolds numbers show the standard "thumb" curve on the cone. The higher frequencies at the beginning of the cone detune rapidly in the narrow amplified band but, as the disturbance waves proceed more downstream, they become better tuned to the boundary layer thickness and amplify at important rates on longer periods of growth. As a consequence, the resulting amplified boundary layer instabilities can potentially reach high amplitude on the cone potentially leading to the critical breakdown amplitude for moderate to high Reynolds numbers.

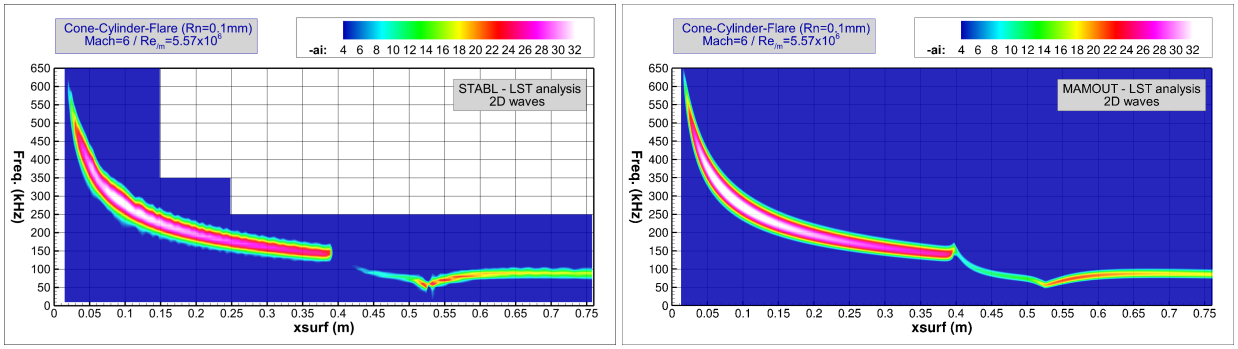

(a) STABL at $Re_{/m}$ = 5.57x10^6 **(b) Mamout at $Re_{/m}$ = 5.57x10^6**

Fig. 8 Amplification rates from STABL and Mamout LST analyses

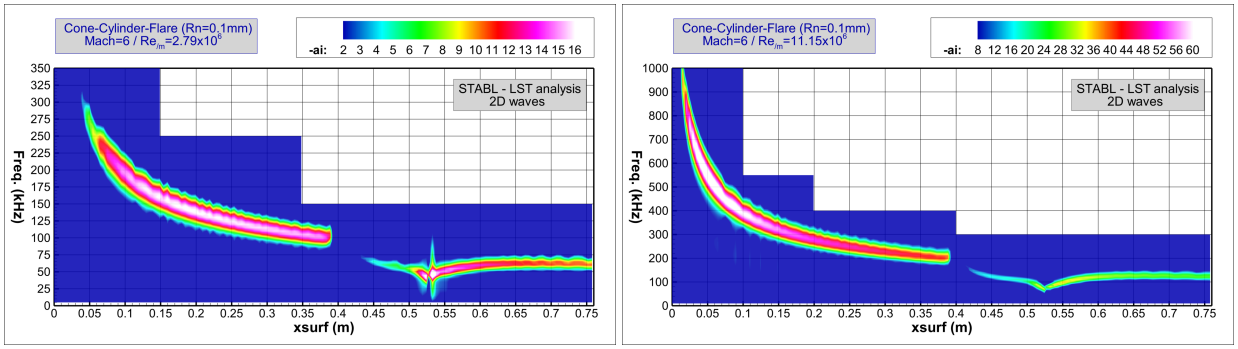

(a) STABL at $Re_{/m}$ = 2.79x10^6 **(b) STABL at $Re_{/m}$ = 11.15x10^6**

Fig. 9 Amplification rates from STABL-LST analyses

Concerning the cylinder part, it is known that a favorable pressure gradient has a stabilizing effect on the boundary layer. This is definitively confirmed by the stability diagrams where no substantial amplification rates are visible on the main part of the cylinder. As shown in figures 6 and 7, the boundary layer thickens very rapidly under the influence of the flow expansion and experiences a very rapid change all along the cylinder. The "accelerated" boundary layer is very stable as confirmed by the amplfication rate diagrams.

The phenomenon is totally different on the flare and it is interesting to remind here that adverse pressure gradients are commonly known as destabilizing for the boundary layer. As visible in figures 6 and 7, the boundary layer thins rapidly just after the cylinder-flare junction but, once the pressure gradient past, the boundary layer keeps a quite constant thickness and a quite identical profile all along the flare. As a consequence, it can be guessed that, after an important destabilization at the cylinder-flare junction, a quite amplified frequency "plateau" could be observed on the flare. It is confirmed by figures 8 and 9 for the all the Reynolds numbers considered here. The amplified waves stay in a narrow frequency range on the flare which can potentially generate high amplitude disturbances at the end of the flare.

All these general trends are confirmed for all the Reynolds number and with the code-to-code comparison, STABL / Mamout, which points out a good agreement between these two numerical approaches. This verification gives an even larger confidence in the numerical stability predictions.

The Reynolds effect on the amplification of the second-mode frequency waves is clearly highlighted by figure 9. The large increase of the boundary layer thickness in the case of the lower Reynolds number leads to low frequency range for the second mode amplification: 100-300 kHz on the cone and a narrow band around 50-60 kHz on the flare. The higher Reynolds number considered leads logically to high frequency content: 200 to 1000 kHz on the cone and a long flat frequency range on the flare around 120-130 kHz with important amplification rate levels.

An additional focus is proposed for the case at $Re_{/m}$ =5.57x10^6 in the next figures. The extract from SATBL and Mamout in figure 10 indicate the amplification rates of the waves at different frequencies and propagation angles on the cone at x=0.1m. The first-mode is visible for oblique waves with a maximum amplification detected at around 40 kHz and $\psi \sim 65 - 70^o$. The second-mode is, as expected, clearly the dominant mode with a maximum amplifcation rate for the two-dimensional waves ($\psi \sim 0^o$) at frequencies around 260-280 kHz.

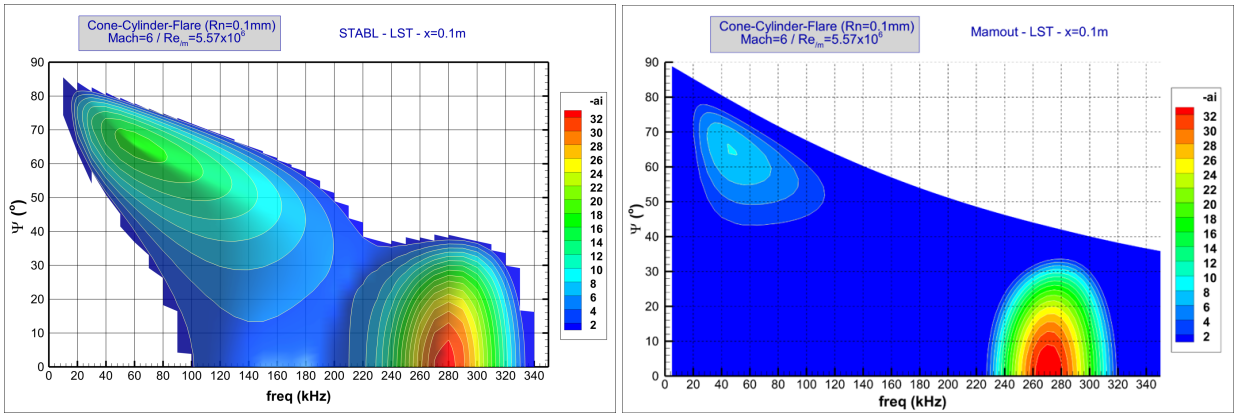

(a) STABL at $Re_{/m}$ = 5.57x10^6 **(b) Mamout at $Re_{/m}$ = 5.57x10^6**

Fig. 10 Amplification rates by frequency and waves propagation angles at $Re_{/m}$ =5.57x10^6

The figure 11 shows the amplification rates at three different locations respectively on the cone, on the cylinder and on the flare. As detailed by Arnal [20], these stability diagrams indicate that first-mode and second-mode are simultaneously present. The amplification rates confirm the dominance of the higher frequency second-mode for two-dimensional waves ($\psi = 0^o$) whatever the considered location on the configuration. The first-mode instabilities are most amplified as oblique waves with sensible levels obtained for wave propagation angle between 50^o and 80^o.

A more quantitative comparison between STABL and Mamout for the streamwise wavenumber and the maximum

amplification rate prediction at three different locations on the object is provided in figure 12. The predicted wavenumbers are quite exactly the same with the two codes. For the amplification rates, the agreement between the 2 codes is very satisfying on the cone and on the flare. On the cylinder, the most amplified frequencies correspond very well but the waves are more amplified with STABL. It seems that the influence of the pressure gradient is felt "stronger" by STABL in comparison to Mamout. A slight difference can be also observed in the low frequency content corresponding to the small amplification levels of the two-dimensional first-mode waves.

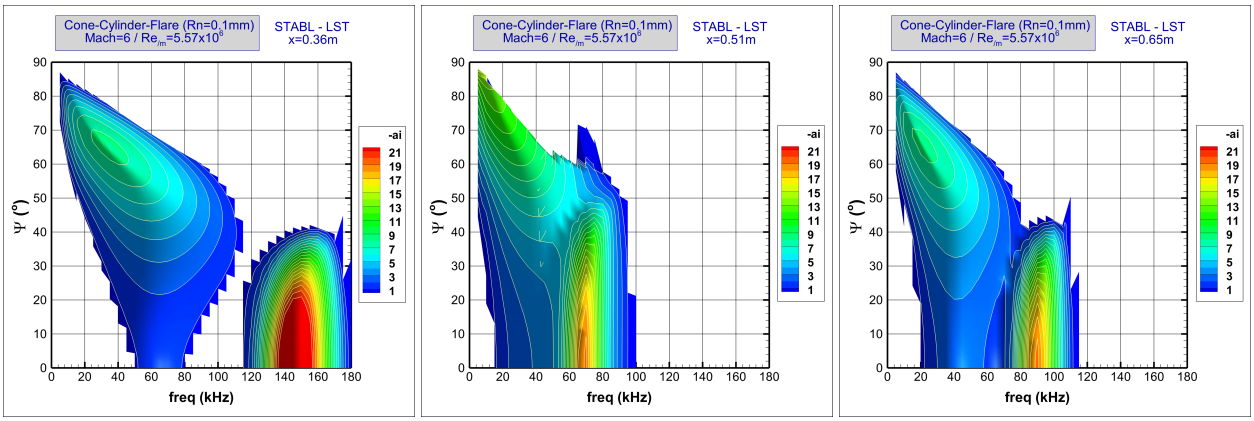

(a) STABL at $Re_{/m}$ = 5.57x10^6 - x=0.36m (b) STABL at $Re_{/m}$ = 5.57x10^6 - x=0.51m (c) STABL at $Re_{/m}$ = 5.57x10^6 - x=0.65m

Fig. 11 Amplification rates by frequency and waves propagation angles at $Re_{/m}$ =5.57x10^6

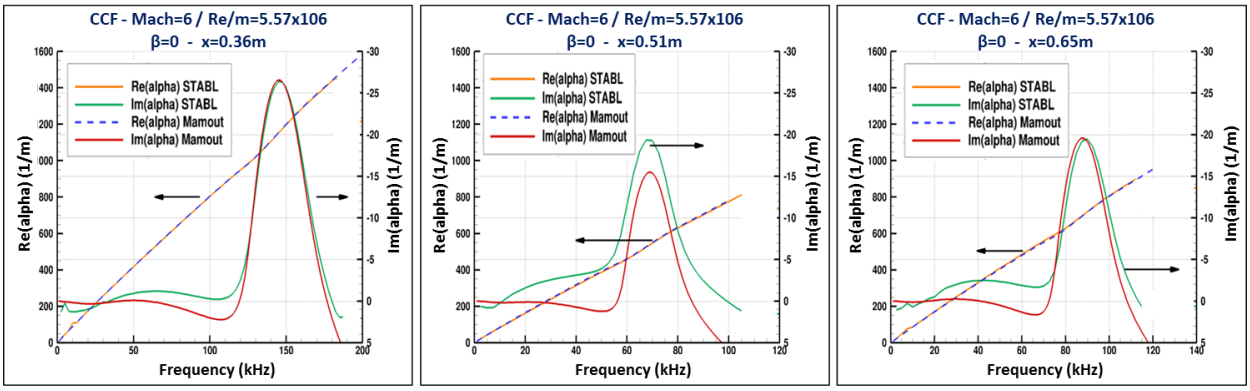

Fig. 12 Wavenumber and maximum amplification from STABL and Mamout in LST mode at $Re_{/m}$ =5.57x10^6

*2. **Second-mode instabilities: trapped acoustic waves***

As explained by Fedorov [17] and Knisely [21], the second-mode disturbances belong to the family of trapped acoustic waves. Indeed, a region of supersonic mean flow relative to disturbance phase velocity is present in the upper part of the boundary layer while, in the lower part of the boundary layer, the disturbances are supersonic relative to the mean flow. As a consequence, this small region near the wall acts as an acoustic waveguide where the waves are trapped. Acoustic rays are reflected by the wall and can not cross the sonic line. The second-mode waves developing in this near-wall region represent inviscid instabilities of acoustic nature which become the dominant instability in hypersonic flow. This supersonic disturbance region can be represented by plotting the relative Mach number defined as:

$$M_r = \frac{\bar{u} - c_r}{\bar{a}}$$

where $\bar{u}$ is the mean flow velocity, c_r is the disturbance propagation speed and $\bar{a}$ is the mean flow speed of sound.

The region where the waves travel downstream supersonically relative to the mean flow is illustrated in figures 13, 14 and 15 respectively at the end of the cone, in the middle of the cylinder and at the end of the flare for a given phase velocity wave equal to 800 m/s. The supersonic region is very thin. The associated pressure disturbance has a maximum at the wall and decreases very rapidly in this supersonic region.

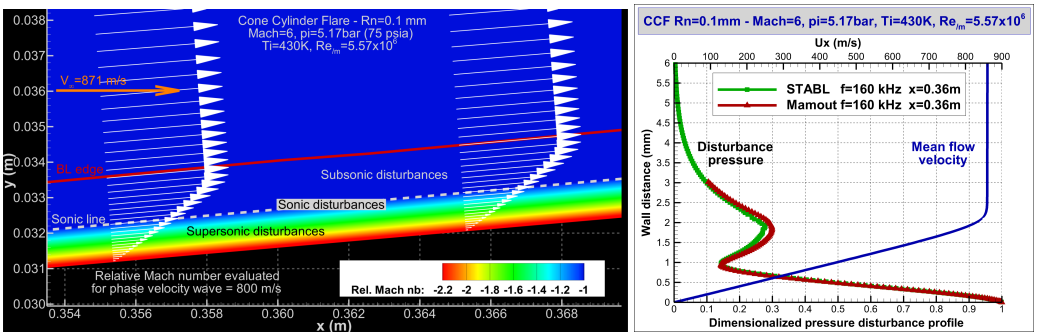

(a) Relative Mach number **(b) Pressure disturbance profile**

Fig. 13 Relative Mach number and pressure disturbance profile at the end of the cone ($Re_{/m}$ = 5.57x10^6)

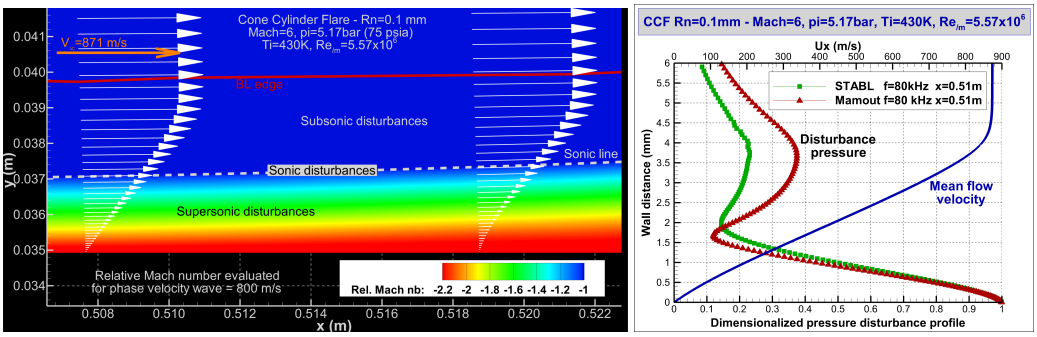

(a) Relative Mach number **(b) Pressure disturbance profile**

Fig. 14 Relative Mach number and pressure disturbance profile at the end of the cylinder ($Re_{/m}$ = 5.57x10^6)

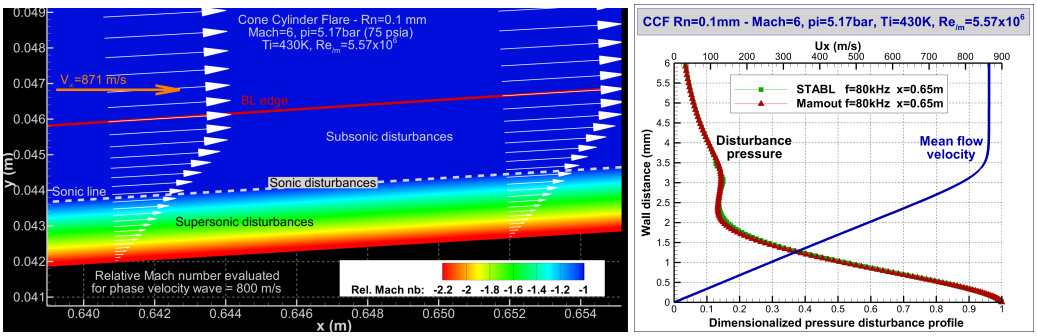

(a) Relative Mach number **(b) Pressure disturbance profile**

Fig. 15 Relative Mach number and pressure disturbance profile in the middle of the flare ($Re_{/m}$ = 5.57x10^6)

The disturbance profiles obtained with STABL and Mamout confirm that the main part of the second-mode lies below the sonic line (as also shown by Chen et al. [22]) while the trace of the first-mode (2D waves only here) is visible near the boundary layer edge close to the generalized inflection point. The high speed flow regime considered here leads

logically to the dominance of the compressibility effects when compared to the viscous effects. As a consequence, the second-mode is more unstable than the first-mode even if we consider the most-amplified oblique first-mode waves at $55 - 60^o$ (see figure 11). The second-mode disturbance peak is located at the wall, this represents a very useful advantage to measure the amplitude of the second-mode waves by wall pressure measurements.

3. N-factors

Knowing the evolution of an initial disturbance as it moves downstream from its starting point through the mean flowfield, the onset of transition can be estimated with the semi-empirical e^N correlation method. In PSE-Chem, the N factor is defined as:

$$N = \int_{s_0}^{s} [-\alpha_i + \frac{1}{2E}\frac{dE}{ds}]ds$$

where not only the imaginary component of the streamwise wavenumber is taken into account (as in LST) but also the change in the kinetic energy of the shape function.

With this integrated growth of the linear instability waves, it is possible to correlate the onset of transition using N-factor values of about 8-11 for quiet tunnel and flight environments and levels around 4 to 5 for conventional tunnels with larger freestream noise environment.

Figure 16 shows the N factor distribution along the ccone-cylinder-flare configuration at $\mathrm{Re}_{/m}$ =5.57x10^6 obtained in PSE mode for the two-dimensional disturbances only (ψ= 0°). The wave amplitude increase on the cone is "classical" and well correlated with the boundary layer thickness. The maximum amplitude of the waves increases when the frequency decreases and the greatest N factor on the cone is obtained for 160 kHz (see also figure 18). The disturbances are damped by the flow expansion occuring at the cone cylinder junction. The amplitude of low frequency disturbances start to increase on the second part of the cylinder and some of them are amplified a new time on the flare leading to high N factor levels at the end of the configuration for a very narrow frequency range (80-90 kHz).

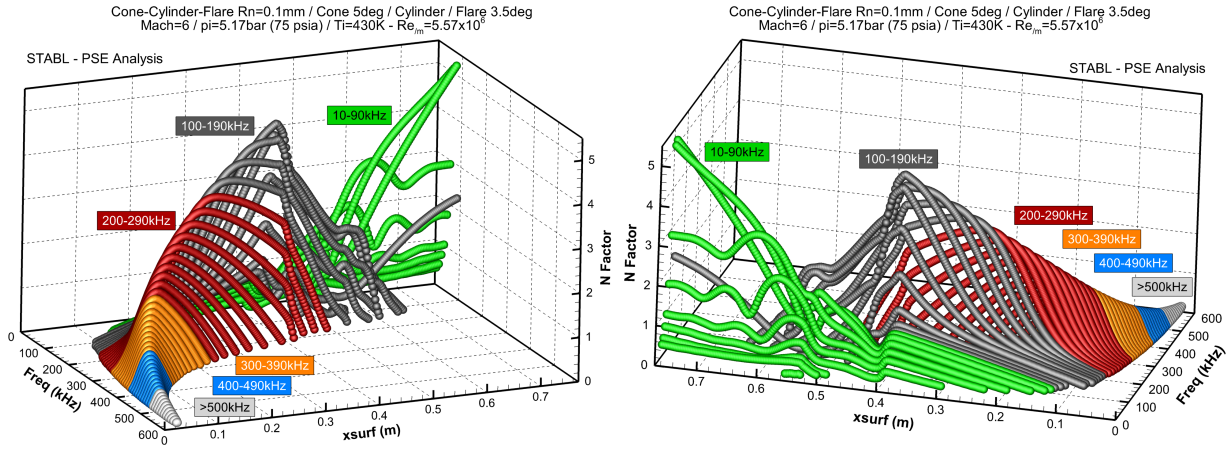

(a) N factor evolution at $\mathrm{Re}_{/m}$ = 5.57x10^6 - View 1 **(b) $\mathrm{Re}_{/m}$ = 5.57x10^6 - View 2**

Fig. 16 N factor evolution along the object from STABL-PSE analysis at $\mathrm{Re}_{/m}$ = 5.57x10^6

For this intermediate Reynolds number, N factors slightly lower than 5 are reached at the end of the cone and slightly greater than 5 at the end of the model. Such N factors values can conduct to turbulent breakdown in a noisy environment while quiet experiments should detect important waves amplitudes before critical laminar-to-turbulent breakdown.

The integrated N factors for the two other Reynolds numbers, $\mathrm{Re}_{/m}$ = 2.79x10^6 and $\mathrm{Re}_{/m}$ = 11.15x10^6, are shown in figure 17 and 19. The general trend is the same as the previous one with a remarkable N factor increase along the cone and along the flare but for totally different frequencies. This frequency change can be related, at first sight, to the very

different boundary layer thickness for these two cases as shown in figure 6a.

At $Re_{/m}$ = 2.79x10^6, the maximum wave amplitude is limited with N factor values just below 3 at the end of the cone and at around 3.6 at the end of the flare. From an experimental point of view, these levels are probably too low to be detected in quiet conditions but measurements can be considered in noisy conditions for this case.

At $Re_{/m}$ = 11.15x10^6, high N factor values are reached: around 8 at the end of the cone and almost 9 at the end of the flare. This case will be turbulent in noisy conditions but represents an ideal candidate for quiet experiments. Indeed, in quiet tunnel conditions, without noise radiated from the boundary layers on the nozzle walls, this case will generate critical wave amplitudes, very near to transition breakdown or possibly turbulent at the end of the configuration.

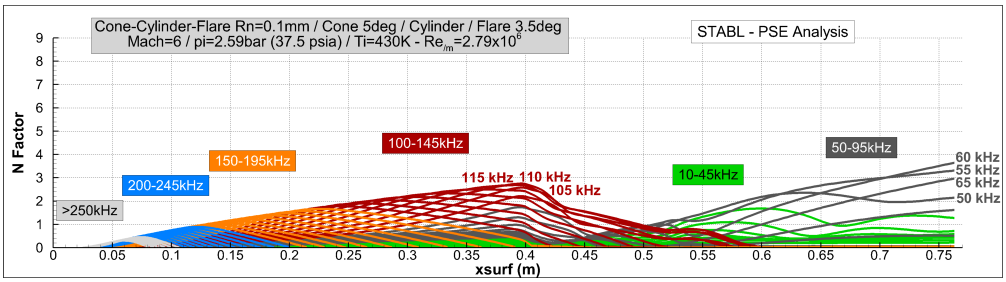

Fig. 17 N factors by frequency from STABL-PSE analysis at $Re_{/m}$ = 2.79x10^6

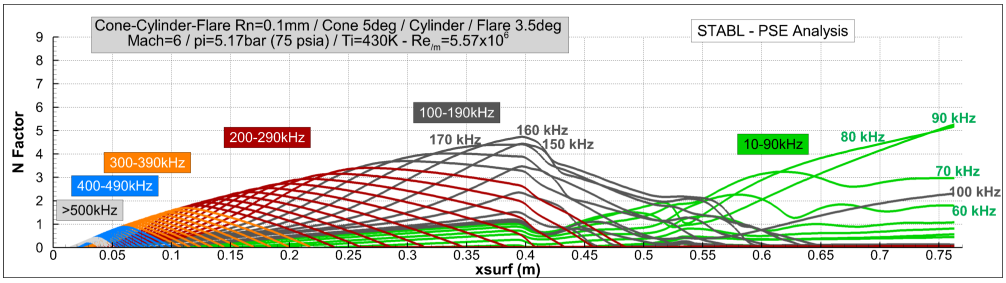

Fig. 18 N factors by frequency from STABL-PSE analysis at $Re_{/m}$ = 5.57x10^6

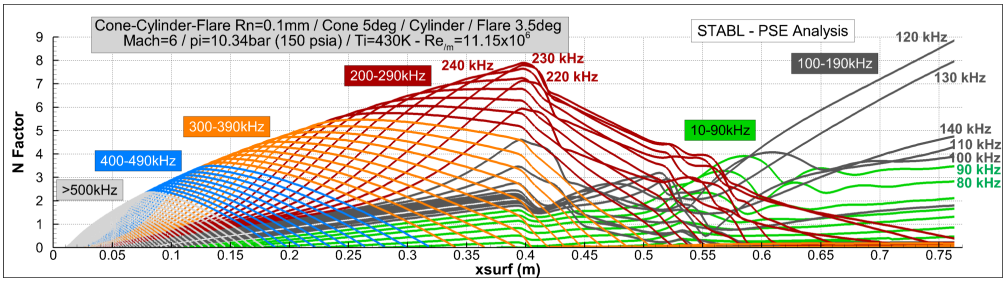

Fig. 19 N factors by frequency from STABL-PSE analysis at $Re_{/m}$ = 11.15x10^6

At this point of the paper, the flow and the stability analysis of the hypersonic boundary layer on the cone-cylinder-flare configuration have been presented in detailed for three Reynolds number. In parallel of this numerical study, experiments have been realized in the BAM6QT wind tunnel on this shape. Several runs have been obtained respectively in noisy and in quiet conditions. In order to compare the previous numerical analysis to experimental results, three runs as close as possible to the previous computational conditions have been selected. These comparisons will be presented in the next chapter respectively for two noisy runs obtained at conditions near the low and medium Reynolds numbers, and for one quiet run realized at the highest Reynolds number investigated in the numerical study.

VII. Model and BAM6QT Experiments

The ccone-cylinder-flare model has been produced in the Aerospace Sciences Laboratory of Purdue University. Experimental tests of this configuration were conducted in Purdue University's Boeing/Air Force Mach 6 Quiet Tunnel.

A. Ccone-cylinder-flare model

As indicated previously, the model tested consists of a 5 degrees half-angle cone leading to a cylinder, followed again by a 3.5 degrees half-angle straight conical flare. The nose tip was made to be as sharp as could be produced with a nose radius equal to 0.1mm based on microscope visual inspection. As a reminder, the main dimensions of the ccone-cylinder-flare configuration are given in table 1.

The model is divided into three sections: a stainless steel nose tip, an aluminum mid-body containing the initial 5 degrees cone and the first half of the cylinder, and an aluminum base including the latter half of the cylinder and the 3.5 degrees conical flare. The intersection of the cylinder with the 3.5 degrees cone presents a compression corner to the oncoming flow. 11 sensor holes are located along the centerline of the model, with 3 additional holes located azimuthally around the first cone to help zero the angle of attack of the model.

The majority of the third section of the model was coated with temperature sensitive paint (TSP) to study the heat transfer and temperature variations caused by the compression corner. All 14 sensor holes were utilized, with all but one being occupied by PCB 132B38 pressure sensors. The remaining hole contains a Schmidt-Boelter 8-1-0.25-48-20835TBS heat transfer gauge used to calibrate the temperature sensitive paint. Figure 20 displays the installed model with the locations and types of each sensor highlighted.

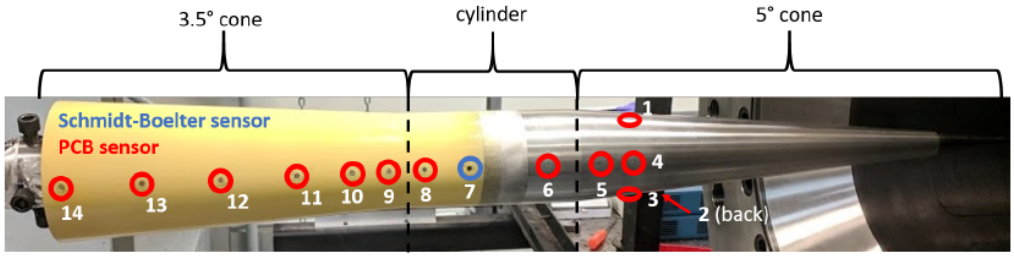

Fig. 20 Purdue model with 9 PCB sensors for BAM6QT experiments

The 13 PCB pressure sensors are used to record second-mode instabilities and 1 Schmidt-Boelter gauge is used to measure the wall temperature. The sensor locations are indicated in table 3.

Table 3 Sensor locations on the configuration

	PCB 1-4	PCB 5	PCB 6	S-B 7	PCB 8
Section	Cone	Cone	Cylinder	Cylinder	Cylinder
x (m)	0.361	0.387	0.425	0.479	0.511

	PCB 9	PCB 10	PCB11	PCB 12	PCB 13	PCB14
Section	Flare	Flare	Flare	Flare	Flare	Flare
x (m)	0.536	0.562	0.600	0.651	0.702	0.752

B. Boeing / AFOSR Mach-6 Quiet Tunnel

The BAM6QT is a Ludwieg tube, a long tube with a converging-diverging nozzle on the end (see figure 21). The flow passes from the driver tube, through the test section, diffuser, a second throat, and finally to the vacuum tank.

BAM6QT can be operated as a conventional noisy tunnel or as a quiet tunnel. Flow is initiated by bursting a double diaphragm that is located downstream of the diffuser. Run times of 3-5 s are typical at present. The tunnel uses air as the test gas and operates with an initial stagnation pressure of 34-2070 kPa (0.34-20.7 bar) and an initial stagnation temperature of 430 K, giving a $Re_{/m}$ range of 0.36-22.3 x 10^6.

The test-section diameter is 0.241 m at the nozzle exit, and the nozzle is 2.590 m long. It is difficult to obtain quiet flow in a hypersonic tunnel. The nozzle is polished to a mirror finish to avoid roughness-induced transition. The contraction boundary layer is also removed by bleed slots at the throat for quiet runs. A new laminar boundary layer begins just upstream of the nozzle throat and is maintained through the test section. The air is filtered to remove dust or other particles above 0.01-microns that may damage the nozzle or trip the boundary layer. More details about the development of the BAM6QT can be found in [11].

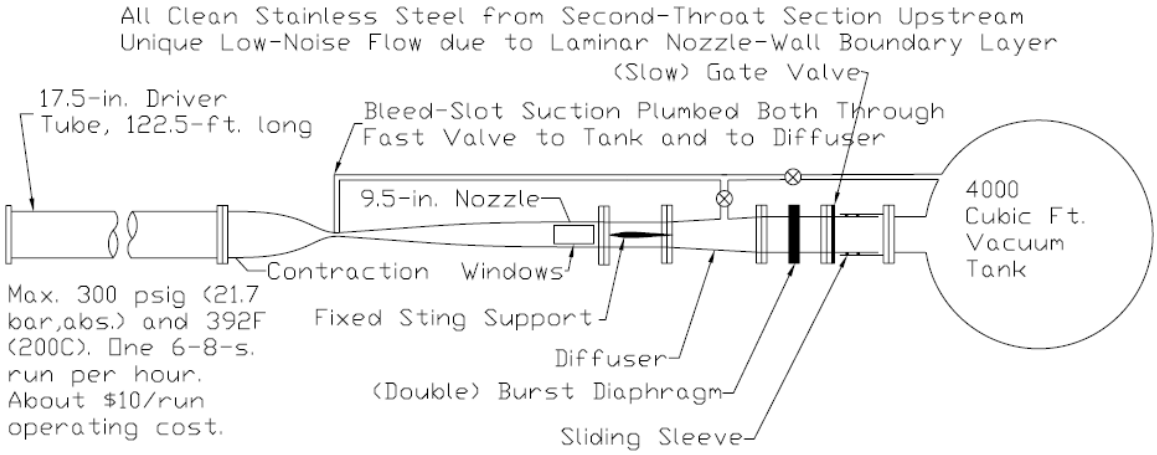

Fig. 21 Schematic of Boeing/AFOSR Mach 6 Quiet Tunnel

C. Comparison of STABL analyses and BAM6QT measurements

*1. **Noisy runs***

Several noisy runs have been obtained during the wind tunnel test campaign. Two runs are considered for the numerical / experimental comparison respectively at $Re_{/m}$ = 3.31x10^6 and $Re_{/m}$ = 6.00x10^6. In noisy environment, the experimental Mach number is equal to 5.8 because of the larger turbulent boundary layer thickness which develops on the nozzle walls in these conditions. The corresponding aerodynamic conditions are given in Table 4:

Table 4 Aerodynamic conditions

Run	Mach	pi (bar/psia)	Ti (K)	$Re_{/m}$	p_∞ (Pa)	T_∞ (K)	ρ_∞ (kg/m^3)	V_∞ (m/s)
Run25	5.8	2.85 / 41.3	430.	3.31x10^6	222.1	55.6	0.01391	867.3
Run18	5.8	5.17 / 75.0	430.	6.00x10^6	403.0	55.6	0.02523	867.3

These aerodynamic conditions are not exactly the ones corresponding to the numercial cases presented previously in the paper at Mach 6, so new STABL computations have been performed at Mach 5.8.

Figures 22 and 23 show comparisons of measured power spectra with computed N factors. Indeed, N factor correspond roughly with wave amplitude since it is a representation of how much a wave has grown along the body (Berridge et al. [23]). The initial amplitude of the wave is not known so this N factor can not give an absolute wave amplitude. Nevertheless, an interesting numerical / experimental analogy can be made by adjusting manually the maximum N factors to fit the maximum power spectra value. This kind of plot has another advantage: if the stability

computation is accurate and if 2^{nd} mode waves are detected by the experiments, the peaks of amplified instability should be at the same frequencies. In this case, if the computational and experimental frequencies match, no doubt the detection of the waves is correct. Figures 22 and 23 display such N factor / power spectra comparison for the two noisy runs considered here. The overall agreement is correct and the following analysis can be made.

On the cone, 2^{nd} mode waves can be seen on each PCB sensor location (x = 0.361 m and x = 0.387). The large peaks are centered respectively at around 140 and 130 kHz for the lower Reynolds number and at around 160 and 170 kHz for the larger Reynolds number. A slightly larger amplitude is logically observed at the second PCB location. A correct agreement is obtained with the STABL N factors adjusted manually to fit with the experimental power spectra. At the second sensor position, the N factor value is equal to almost 3 at $Re_{/m}$ = 3.31x10^6 and to 4.6 at $Re_{/m}$ = 6.00x10^6. For these noisy runs, the power spectra indicate that the boundary layer remains laminar on the cone in these conditions. A new increase of the Reynolds number (above 6 millions) should lead to a turbulent spectrum knowing that the onset of transition can be estimated using N factor values around 4 to 5 for conventional noisy runs.

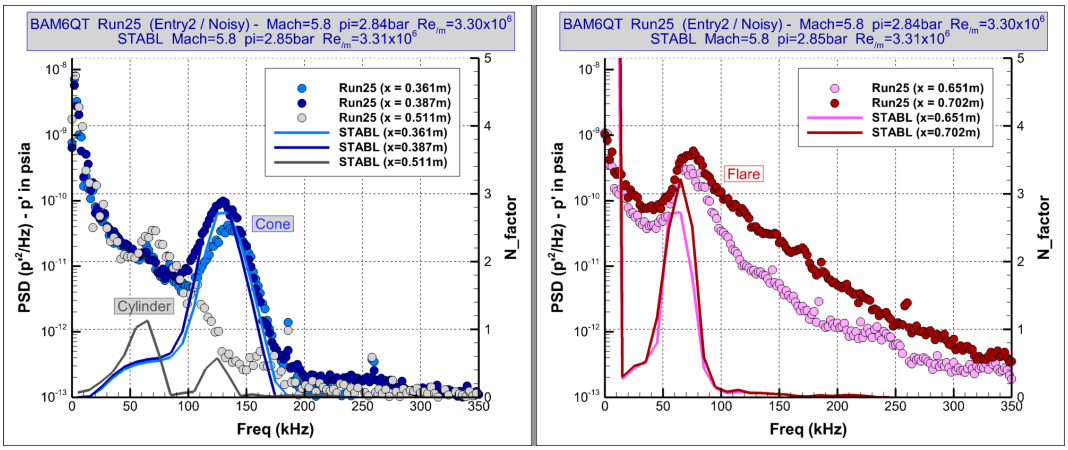

Fig. 22 Comparison of BAM6QT PSD data for noisy run 6 and STABL N-factors at $Re_{/m}$ = 3.3x10^6

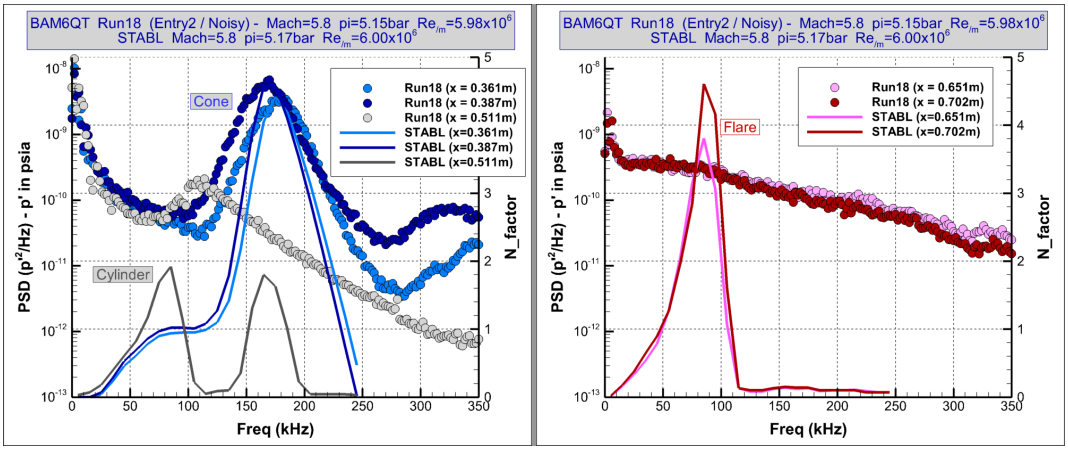

Fig. 23 Comparison of BAM6QT PSD data for noisy run 18 and STABL N-factors at $Re_{/m}$ = 6.0x10^6

On the cylinder part, the computed / experimental comparison is not as evident as on the cone. At the considered PCB location (x=0.511 m) just before the end of the cylinder, two peaks can be observed on the N factor prediction but only one on the power spectra. Furtermore, the N factor and PSD levels do not fit. The figure 24 allows to explain the two peaks computed with STABL at $Re_{/m}$ = 6.0x10^6. The first peak at around 170 kHz comes form the second-mode waves highly amplified on the cone and progressively damped on the cylinder part. The second peak corresponds to lower frequencies at around 70-90 kHz amplified along this second section of the object. The peak detected in the

experiment is at 110 kHz so at a higher frequency than the numerical prediction. If the model was not accurately at 0 degree angle of attack, this could partly explain this scatter but a double check confirms that it is very near from 0 degree. No explanation is available about this point and the measured / computed comparison is unconclusive on this cylinder part.

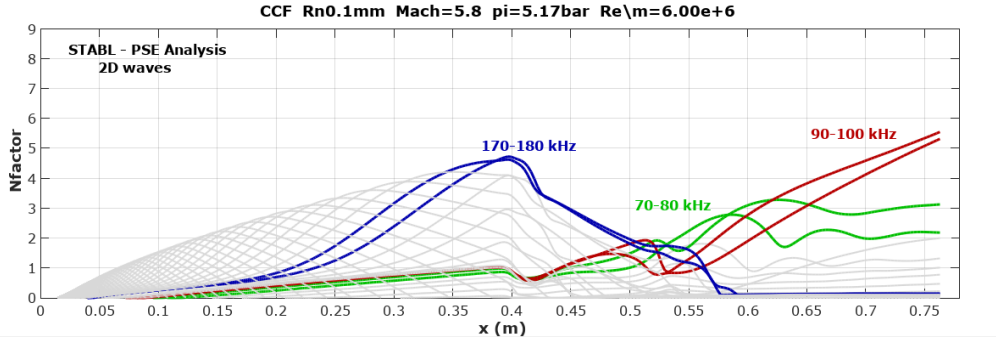

Fig. 24 STABL N factors corresponding to BAM6QT noisy run 18 at $Re_{/m}$ = 6.0x10^6

On the flare, the boundary layer is laminar at $Re_{/m}$ = 3.31x10^6 with experimental 2^{nd} mode peaks observed at around 70 and 75 kz. The computed frequencies are at a slighty lower frequency but second-mode waves are clearly identified here by the computed and experimental approaches. For the second run at $Re_{/m}$ = 6.00x10^6, the PCB measurements indicate a turbulent spectrum on the flare while the stability analysis indicates N factors at around 4.5 for wave frequencies around 90 kHz for both sensors (x=0.651 m and x=0.702 m). In noisy conditions, such N facor values are indeed near to transition or turbulent. Here the flow has become turbulent on the flare even if the predicted N factor is slightly lower on the flare than on the cone - this fact is questionable and this situation is not fully explained at this moment. One possible explanation could come from the one discussed by Marineau in [6]: in experiments an increased tunnel noise exists at lower frequencies while a decreased tunnel noise is observed at high frequency. So the transition could appear firstly on the lower frequency band on the flare than on the higher frequency band on the cone.

*2. **Quiet runs***

New quiet runs have been realized very recently. The purpose of these tests was to obtain experimental data to compare with STABL instability computations. One very interesting case is the one performed at the highest Reynolds number i.e $Re_{/m}$ = 11.15x10^6. The aerodynamic conditions corresponding to this case are reminded in table 5 :

Table 5 Aerodynamic conditions

Run	Mach	pi (bar/psia)	Ti (K)	$Re_{/m}$	p_∞ (Pa)	T_∞ (K)	ρ_∞ (kg/m^3)	V_∞ (m/s)
Run28	6.0	10.34 / 150.0	430.	11.15x10^6	654.9	52.4	0.04351	871.0

The N factors evaluated along the configuration are displayed in figure 19 presented previously. The maximum N factor values are above 8 on the cone and near 9 at the end of the flare. It is important to notice that only quiet runs can measure such amplified instabilities ; this flow would be turbulent at this Reynolds number in all conventional wind tunnels.

Figure 25 shows the experimental and computational results obtained for run 28. Figure 25a displays the power spectra for each PCB sensor but PCB 2 and PCB 14 broke during the test campaign. Before analyzing the results, it is important to notice that in the experimenal data, every PCB sensor contains a peak at around 124 kHz. As we will explain below, this frequency is physical on the flare but not on the cone nor on the cylinder. It is uncertain the cause of these peaks. Nevertheless, these data are very interesting and a useful analysis can be realized by comparing these experimental results with the numerical analysis.

For PCBs 1, 3, and 4, which are located azimuthally around the first cone at the same axial position downstream, the fluctuations peak at frequencies of 237 kHz, 235 kHz, and 236 kHz, respectively. This frequency agreement confirms the very near zero angle of attack of the model during the test. Downstream of these sensors, PCB 5 peaks at 229

kHz. The 2^{nd} mode is clearly identified by these sensors on the cone, the slightly reduced frequency for PCB 5 is due to the increase of the boundary layer thickness between these two locations. The measured and computed 2^{nd} mode frequencies compare very well as confirmed by figure 25b. The N factor values peak at high levels, 7.3 and 7.7 respectively, at the considered x-location on the cone (x=0.361 m and x=0.387m). The N factor is equal to 8 at the end of the cone (see figure 19 and 26).

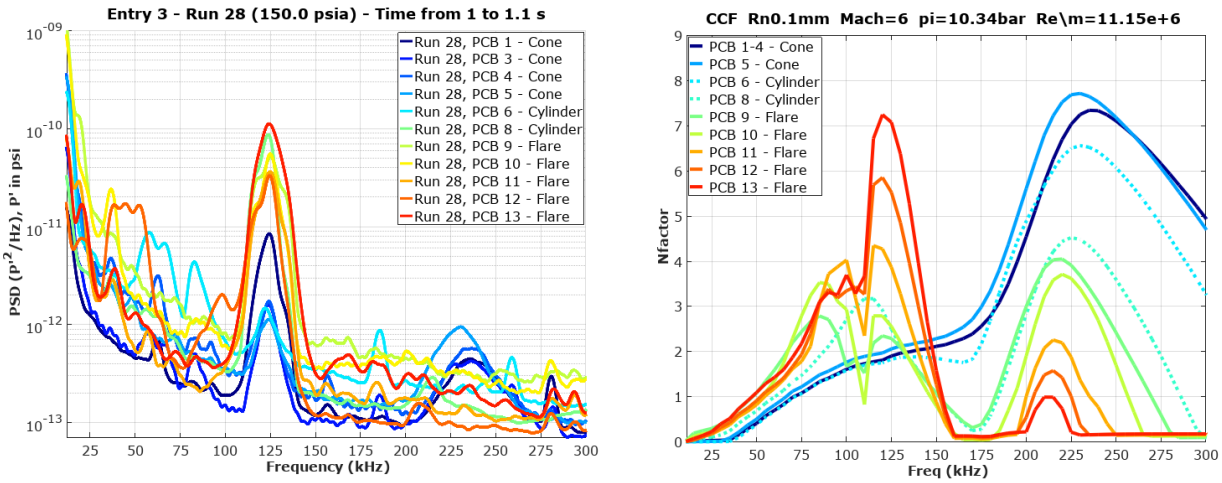

(a) Power spectra from the PCB sensors **(b) Computed N factors at the sensor locations**

Fig. 25 Power spectra from BAM6QT and computed N factors from STABL at $Re_{/m}$ = 11.15x10^6

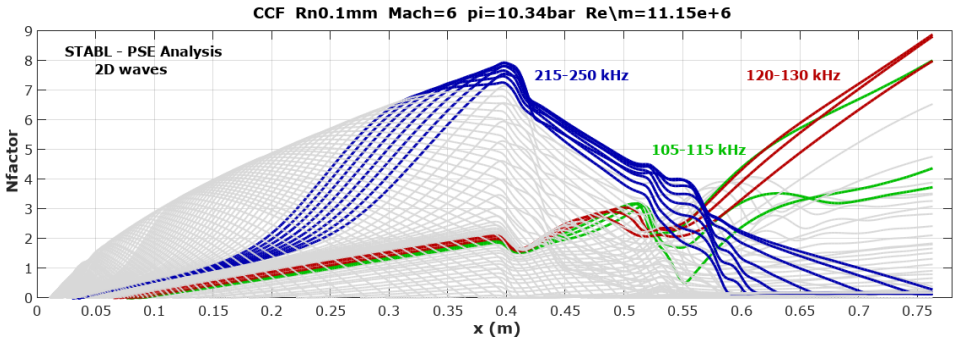

Fig. 26 STABL N factors corresponding to BAM6QT quiet run at 150 psia

On the cylinder part, as indicated previously, the stabilizing effect of the flow expansion leads to very limited amplification rates as shown in figure 9. In this zone where the boundary layer thickness rapidly increases and where the boundary profile is strongly modified (see figure 7), the instabilities are damped on the first part of the cylinder and amplified on the rear part but at much lower frequencies than the one on the cone. The PCB measurements are not conclusive for this case on the cylindre part. Concerning the stabiltiy analysis, the computed N factors show one peak at the first PCB location and two peaks at the second location. The high frequency peak at around 225 kHz is due to the remaining but progressively damped 2^{nd} mode waves initially generated upstream on the cone as shown in figure 26. The second peak visible on PCB 8 is at around 110 kHz. Figure 26 shows that, after a first amplification on the cone, these instabilities are amplified a new time along the cylinder and reach amplitudes corresponding to a N factor around 3.2.

Along the conical flare, the second set of peaks at around 124 kHz, matches very well with the predicted second mode fluctuations. Figure26 displays three interesting discrete frequencies: 120, 125 and 130 kHz which clearly show the evolution of these instabilities along the configuration. After a slight amplification of the 2D waves on the cone and on the cylinder, because of the influence of the compression on the flare, a strong N factor increase is observed. Because

of the quite constant boundary layer thickness and profile in this region, the same limited frequency range is amplified downstream and reaches high N factor values near 9 at the end of the flare. The STABL results indicate N factor values equal to 5.8 and 7.2 for PCB 12 and 13 located respectively at x=0.651 m and 0.702 m. Because of the presence of spikes in the experiment, it is not possible to fit the the maximum power spectra with the maximum N factor levels at the different sensor locations but the agreement on the frequency is very good.

VIII. Conclusion

This cone-cylinder-flare configuration generates a very interesting aerodynamic flow for the study of hypersonic boundary layer stability in presence of pressure gradients. The 5-degree sharp cone leads "classically" to high instability amplification rates at moderate Reynolds numbers but, further downstream, the flow expansion and the compression generated on the cylinder and on the 3.5 degree conical flare lead to important changes of the boundary layer stability.

The STABL stability computations and the BAM6QT wind tunnel data provide new insights about the boundary-layer transition process on this axisymmetric cone-cylinder-flare configuration considered at Mach 6. For this case, at zero angle of attack, the 2^{nd} mode waves are the dominant instabilities. The 1^{st} mode instabilities are still present in the boundary-layer but at a lower amplification rate. For three different Reynolds number, respectively $Re_{/m}$ = 2.79x10^6, 5.57x10^6 and 11.15x10^6, this numerical study has confirmed the stabilizing effect of a favorable pressure gradient and the destabilizing effect of an adverse pressure gradient. Indeed, a rapid damping of the 2^{nd} mode high frequency waves (generated upstream on the cone) is predicted on the first half of the cylinder. On the second half, because of an important increase of the boundary-layer thickness, another range of lower frequency instabilities is slightly amplified. On the flare, the stability computations show amplified waves in a narrow and quite constant frequency range conducting to high 2^{nd} mode wave amplitudes at the end of the configuration. Following this amplification pattern, the highest N factor values are obtained at the end of the cone and at the end of flare but for totally different frequencies. At the highest Reynolds number considered here, $Re_{/m}$ = 11.15x10^6, the N factor is equal to around 8 at the end of the cone and to around 9 at the end of the flare for 2^{nd} mode wave frequencies respectively equal to 230-240 kHz and 120-130 kHz.

Numerical / experimental comparisons have been realized for two intermediate Reynolds number, around 3 and 6 millions, in noisy conditions and for a higher Reynolds number, around 11 millions, in quiet conditions. The measured and computed 2^{nd} mode frequencies compare very well on the cone and on the flare. The comparison on the cylinder part is more uncertain. Some questions are still open but the present study provides new insights in the physical description of the transition process on a configuration with favorable and adverse pressure gradients in hypersonic regime.

As a perspective, it can be said that new wind tunnel / stability analyses comparisons at complementary Reynolds numbers could provide useful additional information for an in-depth transition description. It can also be stated that this new cone-cylinder-flare configuration appears as a very good basis for complementary studies, such as the study of bluntness effect on transition by considering different nose radius or also for the study of flow separation influence on transition by increasing the flare angle.

IX. Acknowledgments

Sebastien Esquieu thanks Professor Steven P. Schneider for hosting him in the Aerospace Sciences Laboratory and for his continuous guidance during the internship. Thanks as well to Elizabeth Benitez for providing the wind tunnel test data and for all the fruitful discussions about the numerical / experimental comparisons. Many thanks are due to Heath Johnson from University of Minnesota for the access to the STABL suite and to Jean-Philippe Brazier for the technical exchanges about stability analyses. Esquieu thanks also the French DGA for providing him a grant to study abroad. Schneider's efforts were supported by AFOSR Grant FA9550-17-1-0419. Benitez was supported by a NDSEG fellowship.

References

[1] Leyva, I. A., "The relentless pursuit of hypersonic flight," *Physics Today*, Vol. 70, 2017, pp. 30, 36. doi:https://physicstoday.scitation.org/doi/10.1063/PT.3.3762.

[2] Stetson, K. F., "Comments on Hypersonic Boundary-Layer Transition," *Flight Dynamics Laboratory, WRDC-TR-90-3057*, 1990.

[3] Morkovin, M. V., Reshotko, E., and Herbert, T., "Transition in open flow systems: a reassessment," *Bull. Am. Phys. Soc. 39:1882*, 1994.

[4] Schneider, S. P., "Developing Mechanism-Based Methods for Estimating Hypersonic Boundary-Layer Transition in Flight: The Role of Quiet Tunnels," *Progress in Aerospace Sciences*, Vol. 72 (2015) 17-29, 2015.

[5] Casper, K. M., Beresh, S. J., Henfling, J. F., Spillers, R. W., Pruett, B., and Schneider, S. P., "Hypersonic Wind-Tunnel Measurements of Boundary-Layer Pressure Fluctuations," *39th AIAA Fluid Dynamics Conference*, Vol. AIAA Paper 2009-4054, 2009.

[6] Marineau, E. C., Moraru, G. C., Lewis, D. R., Norris, J. D., Lafferty, J. F., and Johnson, H. B., "Investigation of Mach 10 Boundary Layer Stability of Sharp Cones at Angle-of-Attack, Part 1: Experiments," *AIAA SciTech Forum, 53rd AIAA Aerospace Science Meeting, AIAA 2015-1737*, 2015.

[7] Mack, L. M., "Boundary-Layer Linear Stability Theory," *AGARD Report No. 709, Part 3*, 1984.

[8] Benay, R., Chanetz, B., Mangin, B., L., V., and Perraud, J., "Shock Wave/Transitional Boundary Layer Interactions in Hypersonic Flow," *AIAA Journal, Vol. 44, No. 6*, 2006.

[9] Bur, R., and Chanetz, B., "Experimental Study on the PRE-X vehicle focusing on the transitional shock-wave/ boundary layer interactions," *Aerospace Science and Technology 13*, 2009.

[10] Johnson, H. B., and Candler, G. V., "Hypersonic Boundary Layer Stability Analysis using PSE-Chem," *AIAA Paper 2005-5023*, 2005.

[11] Schneider, S. P., "Development of Hypersonic Quiet Tunnels," *Journal of Spacecraft and Rockets*, Vol. 45(4), 641-664, 2008.

[12] Stetson, K. F., "On Predicting Hypersonic Boundary-Layer Transition," *Flight Dynamics Laboratory, AFWAL-TM-87-160-FIMG*, 1987.

[13] Marineau, E. C., Moraru, G. C., Lewis, D. R., Norris, J. D., Lafferty, J. F., Wagnild, R. M., and Smith, J. A., "Mach 10 Boundary Layer Transition Experiments on Sharp and Blunt Cones," *AIAA Aviation Forum, 19th AIAA International Space Planes and Hypersonic Systems and Technologies Conference, AIAA Paper 2014-3108*, 2014.

[14] Bertin, J. J., "Hypersonic Aerothermodynamics," *AIAA Education Series*, 1994.

[15] Wuerer, J. E., "Flow Separation in High Speed Flight - A Review of the State-of-the-Art," *Douglas Report SM-46429, DTIC AD616216*, 1965.

[16] Chynoweth, B. C., "Measurements of Transition Dominated by the Second-Mode Instability at Mach 6," *Doctor of Philosophy Dissertation, Purdue University*, May 2018.

[17] Fedorov, A., "Transition and Stability of High Speed Boundary Layers," *The Annual Review of Fluid Mechanics*, 2011.

[18] Kendall, J. M., "Wind Tunnel Experiments Relating to Supersonic and Hypersonic Boundary Layer Transition," *AIAA Journal, Vol.13, pp.290-299*, March 1975.

[19] Robarge, T. W., and Schneider, S. P., "Laminar Boundary-Layer Instabilities on Hypersonic Cones: Computations for Benchmark Experiments," *35th AIAA Fluid Dynamics Conference and Exhibit, Fluid Dynamics, AIAA Paper 2005-5024*, 2005.

[20] Arnal, D., "Boundary Layer Transition: Predictions Based on Linear Theory," *AGARD-VKI Special course on "Progress in Transition Modelling"*, 1993.

[21] Knisely, C. P., and Zhong, X., "An Investigation of Sound Radiation by Supersonic Unstable Modes in Hypersonic Boundary Layers," *AIAA Paper 2017-4516*, 2017.

[22] Chen, X., Zhu, Y., and Lee, C., "Interactions between second mode and low-frequency waves in hypersonic boundary layer," *J. Fluid Mech. (2017), vol. 820, pp. 693-735*, 1993.

[23] Berridge, D. C., Casper, K. M., Rufer, S. J., Alba, C. R., Lewis, D. R., Beresh, S. J., and Schneider, S. P., "Measurements and Computations of Second-Mode Instability Waves in Three Hypersonic Wind Tunnels," *AIAA Paper 2010-5002*, 2010.